INORGANIC CHEMISTRY FRONTIERS

RESEARCH ARTICLE

View Article Online
View Journal | View Issue

Cite this: *Inorg. Chem. Front.*, 2024, **11**, 7374

A defect pyrochlore-like acentric cubic lead titanium-tellurate crystal exhibiting strong second harmonic generation activity and an extended transparent window†

Tinghui Zhang,[a] Lili Li,[c] Jing Chai,[a] Haitao Zhou,*[b] Ning Ye,[a] Zhanggui Hu,[a] Yicheng Wu[a] and Conggang Li *[a,c]

Received 30th July 2024,
Accepted 11th September 2024

DOI: 10.1039/d4qi01931h

rsc.li/frontiers-inorganic

Non-centrosymmetric (NCS) oxides have attracted considerable attention owing to their versatile applications in the optoelectronic field. However, tailoring oxide-based NCS crystals with a wide transparency range remains a challenge. Here, we present an acentric cubic lead titanium-tellurate crystal $Pb_4Ti_3TeO_{13}$ (PTTO), identified *via* spontaneous crystallization using the traditional pyrochlore structure as a template. Notably, PTTO features a defect pyrochlore-like structure, characterized by the presence of distorted [Ti/TeO_6] octahedra and [PbO_7] polyhedra, endowing it with a strong second harmonic generation (SHG) activity of about 0.4 × $AgGaS_2$. More importantly, the notable merit of heavy elements Pb and Te lies in their inherently low phonon energy, which effectively redshifts the infrared (IR) transmission cutoff edge exceeding 7.6 μm, thereby surpassing the majority of previously reported tellurate-based acentric crystals. Additionally, a combination of theoretical and structural analyses was employed to elucidate the origin of optical activity in PTTO. These findings inspire a way to extend the IR transmittance range of oxide nonlinear optical crystals with enhanced SHG efficiency.

Introduction

Design and synthesis of non-centrosymmetric (NCS) oxides are of great significance in versatile industrial and scientific domains, primarily attributable to their notable stability and exceptional performance in frequency conversion, ferroelectricity, pyroelectricity, and piezoelectricity, among others. In particular, nonlinear optical (NLO) crystals have attracted much attention due to their frequency conversion capability, facilitating the extension of the spectral range of existing lasers, which has found extensive applications such as optical communication, laser processing and laser medical treatment.[1–6] Over several decades, significant progress has been achieved in the exploration of excellent NLO oxide materials. Notable examples include KH_2PO_4 (KDP), $KTiOPO_4$ (KTP), β-BaB_2O_4 (BBO), LiB_3O_5 (LBO) and $KBe_2BO_3F_2$ (KBBF), which have been widely applied spanning the near-infrared (IR), visible, and ultraviolet wavelength regions.[7–11] However, the availability of high-performance materials in the mid-IR range (3–5 μm) remains limited. Presently, commercially available mid-IR NLO crystals are mainly chalcopyrite-type compounds including $ZnGeP_2$, $AgGaS_2$ and $AgGaSe_2$. Unfortunately, these materials undergo several inherent limitations like undesired two-photon absorption and weak laser-induced damage threshold (LIDT). Consequently, there is an increasing need for the fabrication of oxide-based mid-IR NLO crystals with desirable performance.[12–14]

Recent studies have elucidated that the IR transparency cutoff edge of a material relies predominantly on two or multi-phonon absorptions, along with the atomic composition and the intricate interplay among them. For instance, a notable example is $La_3SnGa_5O_{14}$, where the replacement of the B-site element Nb in $La_3Ga_{5.5}Nb_{0.5}O_{14}$ with the Sn element induces a remarkable redshift in the IR transmission cutoff edge (>10 μm). This distinctive shift can be attributed to the larger atomic radius and increased atomic mass of Sn.[15,16] Similarly, a heterovalent substitution strategy implemented in Li_2MTeO_6

[a]*Tianjin Key Laboratory of Functional Crystal Materials, Institute of Functional Crystal, Tianjin University of Technology, Tianjin 300384, China. E-mail: cgli@email.tjut.edu.cn*
[b]*Guangxi Key Laboratory of Superhard Material, China Nonferrous Metal (Guilin) Geology and Mining Co., Ltd., Guilin, Guangxi 541004, China. E-mail: zhouht@aliyun.com*
[c]*State Key Laboratory of Crystal Materials and Institute of Crystal Materials, Shandong University, Jinan 250100, China*

†Electronic supplementary information (ESI) available: Crystallographic data, calculated "flexibility index", PXRD results of the powder before and after melting, EDS data, SHG comparison, and CIF files for PTTO. CCDC 2374242. For ESI and crystallographic data in CIF or other electronic format see DOI: https://doi.org/10.1039/d4qi01931h

(M = Zr, Ti, Sn), where Nb is substituted with heavier elements such as Te and Zr, Ti, or Sn, not only amplifies their LIDT capability but also extends their IR transmission cutoff edge (>6 μm).[17,18] Moreover, remarkably wide transmission windows are also observed in niobium-containing tellurates like $LiNbTeO_5$ and $Cd_2Nb_2Te_4O_{15}$, where the introduction of the heavy element Te contributes to an extended IR transmittance range. Hence, the rational selection of elemental constituents and the interatomic connection mode can effectively diminish phonon frequencies, thereby enhancing the capabilities of wide IR transparency.[19,20]

The pyrochlore structure, characterized by the chemical formula $A_2B_2O_7$, exhibits a diverse range of compositions, where the A site showcases metals with 8-fold coordination and the B site forms distorted $[BO_6]$ octahedra.[21] Notably, the disparity in the radius ratio between A and B elements plays a critical role in determining the structural configuration. This inherent structural flexibility, determined by distinct compositions, provides a versatile platform for designing functional materials.[22,23] Inspired by these ideas, we focus on enhancing the properties of oxides within the $A_2B_2O_7$ system through compositional and structural modifications, achieved by partial or complete substitution of A or B cations. Taking into account the multifunctional effect, the introduction of heavy elements such as Pb and Te with large ionic radii into the A and B sites, respectively, facilitates a broader IR transmission range due to their inherently low phonon energy.[24,25] Moreover, the distortion-active characteristics of Pb–O and Te–O polyhedra further promote the formation of NCS structures. In parallel, the incorporation of Ti^{4+} cations into the B site is of particular interest, as their unique d^0 electronic configuration exhibits a tendency to adopt distorted $[TiO_6]$ octahedral geometries with a highly average distortion magnitude, thereby contributing to the generation of enhanced second harmonic generation (SHG) activity.[26–30] Building upon these insights, we present a rational design approach for a new NCS cubic lead titanium-tellurate crystal, $Pb_4Ti_3TeO_{13}$ (PTTO), by incorporating distorted $[TiO_6]$ octahedra into a system comprising heavy elements Pb and Te with low phonon frequencies with $A_2B_2O_7$ as a template. Notably, PTTO exhibits a defective pyrochlore structure, resulting in a notably wide transmittance window beyond 7.6 μm and a strong SHG intensity of 0.4 × $AgGaS_2$.[31] In this study, we report the synthesis, structural analysis, thermal stability, optical behavior, and electronic structure of PTTO, combining experimental techniques with theoretical calculations.

Methods

Polycrystalline sample synthesis

The PTTO polycrystalline sample was prepared *via* the solid-state reaction process with the chemical reagents of PbO (99.9% purity), TiO_2 (99.9% purity) and TeO_2 (99.9% purity). These raw materials in the stoichiometric ratio were weighed, thoroughly mixed and ground, and then placed in a platinum crucible and subjected to a pre-heating step at 350 °C for 1 day. After the initial heating, the mixture was reground and homogenized, and then heated to 600 °C for an additional 1 day. Finally, the sample was slowly heated to 720 °C and maintained at this temperature for at least 2 days, yielding the target PTTO compound.

Powder X-ray diffraction

The powder X-ray diffraction (PXRD) analysis of PTTO was conducted using a Rigaku SmartLab 9 kW X-ray diffractometer with Cu Kα radiation (λ = 1.5418 Å). The data were collected in 10–70° with a step size of 0.01° and a step time of 2 s. The data were further analysed utilizing FullProf software, which enables the refinement of the results. These refined results were then utilized to ascertain the purity of the sample.

X-ray photoelectron spectroscopy

X-ray photoelectron spectroscopy (XPS) analysis was performed on PTTO samples using an ESCALAB250Xi X-ray photoelectron spectrometer (Thermo Scientific) with an Al Kα source as the excitation source.

Thermal properties

Thermogravimetric (TG) and differential thermal analysis (DTA) of PTTO were conducted on an HTC-4 thermal analyzer. The target sample was heated from 30 °C to 1200 °C at a default rate of 10 °C min^{-1} under a fully N_2 environment.

Single-crystal XRD measurement

The crystal structural data of PTTO were recorded using a Bruker D8 VENTURE CMOS X-ray source with Mo Kα radiation (λ = 0.71073 Å). The data collected were further processed and corrected using APEX III, and then refined using the SAINT program.[32] The SHELXTL crystallographic software was used to resolve the preliminary crystal structure data.[33] The detailed crystallographic data for PTTO are presented in Table S1.† Additionally, Tables S2–S4† provide more extensive information, including atomic coordinates, equivalent isotropic displacement parameters, atomic occupancy factors, bond distances, bond angles, bond valence sums (BVSs) and anisotropic displacement parameters.

Energy-dispersive spectroscopy

To verify the elemental distribution and atomic proportions of the PTTO compound, energy-dispersive spectroscopy (EDS) analysis was performed using a FEI Quanta FEG 250 field emission scanning electron microscope.

Optical spectrum measurements

The ultraviolet-visible-near infrared (UV-vis-NIR) diffuse reflectance spectrum of PTTO was measured using a Hitachi UH4150 spectrophotometer spanning the wavelength region of 300–1800 nm. The experimental energy gap of PTTO was further determined using the Kubelka–Munk formula.[34] The IR spectrum of PTTO was analyzed using a Frontier Mid-IR

FTIR/STA6000-TL9000-Clarus SQ8 transform IR spectrometer in the wavenumber range of 400–4000 cm^{-1}.

Second harmonic generation evaluation

The SHG response intensity of PTTO was evaluated using a laser operating at a wavelength of 2 μm radiation, followed by the Kurtz–Perry method.[35] During the measurement, $AgGaS_2$ of the same size was used as a reference for comparison.

Computational details

To investigate the correlation between structure and performance, the density functional theory (DFT) method was employed to analyze the electronic structure of PTTO.[36,37] The exchange–correlation potential was analyzed using the Perdew–Burke–Ernzerhof (PBE) functional within the framework of the generalized gradient approximation (GGA).[38] The modeling of the interaction between electrons and ionic cores utilized norm-conserving pseudopotentials. To ensure data accuracy, a plane-wave basis with a cutoff kinetic energy of 810 eV was employed, along with a Monkhorst–Pack *k*-point grid of 4 × 3 × 2 for sampling and numerical integration in the Brillouin zone.

Results and discussion

Synthesis and thermal characterization

The PTTO polycrystalline sample was synthesized using the high-temperature solid phase method. The Rietveld profile fitting of the PTTO sample is depicted in Fig. 1a. The characteristic diffraction peaks of PTTO correspond to the standard patterns, indicating its high purity. The thermal behavior of PTTO was assessed by the utilization of DTA–TG analysis. As illustrated in Fig. 1b, the TG and DTA curves demonstrate that PTTO displays excellent thermal stability, with significant endothermic peaks and mass loss observed before 877 °C. Additionally, the PXRD patterns of both the initial and melted PTTO samples exhibit incongruence (Fig. S1†), indicating that PTTO is an incongruently melting compound.

Crystal structure determination

Remarkably, despite the PTTO compound being discovered in 1986, its structure was found to crystallize in the centrosymmetric $Fd\bar{3}m$ space group, in contrast to its unexpected NLO-active behavior.[39] In light of this finding, we undertook a reevaluation to corroborate and validate the structural characterization of the compound. In this work, single crystal XRD reveals that the structure of PTTO closely resembles that of the conventional CS pyrochlore $A_2B_2O_7$. However, PTTO crystallizes in the NCS cubic space group $F\bar{4}3m$ (No. 216) with cell parameters of a = 10.3488(2) Å, b = 10.3488(2) Å, c = 10.3488(2) Å and V = 1108.33(6) $Å^3$. Each asymmetric unit of PTTO contains a unique Pb atom, a unique Ti/Te atom and three unique O atoms. Notably, the Ti and Te atoms occupy the same site in a 3 : 1 ratio, resulting in a disordered structure. As illustrated in Fig. 2a, Pb exhibits coordination with seven O atoms, resulting in the formation of a highly distorted $[PbO_7]$ polyhedron, attributed to the second-order Jahn–Teller effect. In this coordination environment, the Pb–O bond lengths vary significantly, ranging from 2.283(2) to 2.644(6) Å. These $[PbO_7]$ polyhedra are interconnected through edge-sharing interactions, forming the $[Pb_4O_{22}]_\infty$ spatial structural network as displayed in Fig. 2b. The Ti/Te atoms exhibit a disordered arrangement, and they are surrounded by six oxygen atoms, forming a distorted octahedron configuration with the Ti/Te–O bond length range of 1.948(5)–1.961(4) Å. These adjacent $[Ti/TeO_6]$ octahedra are interconnected to each other through edge-sharing oxygens, resulting in the formation of the $[Ti/Te_4O_{18}]_\infty$ spatial network structure (Fig. 2b). Subsequently, the designated $[Pb_4O_{22}]_\infty$ and $[Ti/Te_4O_{18}]_\infty$ clusters are further linked through corner-sharing oxygens, yielding the overall 3D spatial structural framework of PTTO, as depicted in Fig. 2c.

Considering that the crystal structure of PTTO can be regarded as a derivative of the traditional pyrochlore, it is

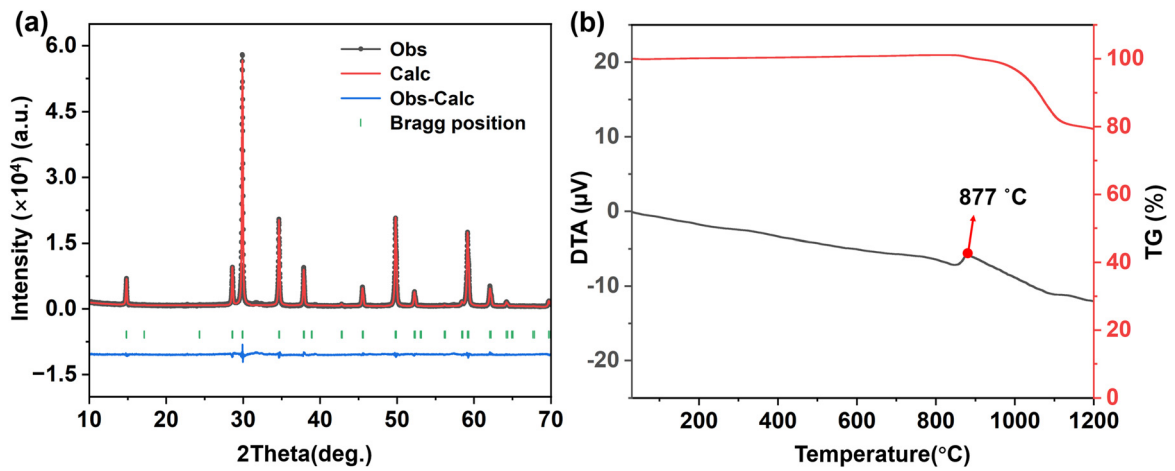

Fig. 1 (a) Rietveld refinement plots of PTTO. (b) DTA and TG curves of the PTTO polycrystalline sample.

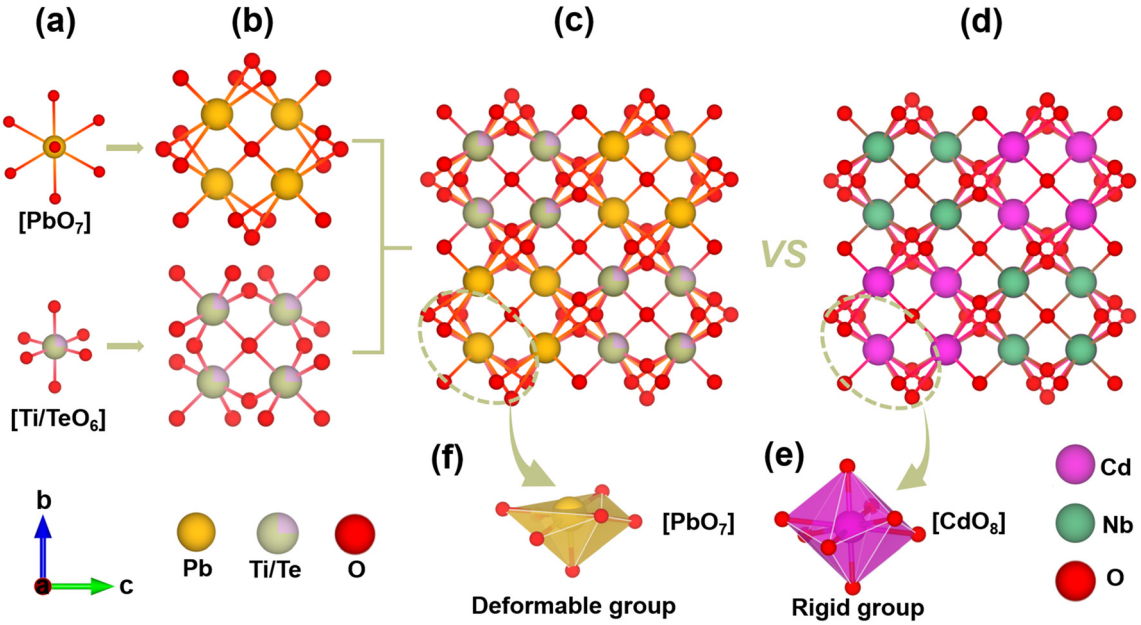

Fig. 2 Structural characterization of PTTO: (a) $[PbO_7]$ and $[Ti/TeO_6]$ motifs. (b) Presentation of $[Pb_4O_{22}]_\infty$ and $[Ti/Te_4O_{18}]_\infty$ fragments. (c) 3D spatial network structure of PTTO. (d) 3D spatial structural network of $Cd_2Nb_2O_7$. (e) Rigid $[CdO_8]$ polyhedra. (f) Distorted $[PbO_7]$ polyhedra.

necessary to make a comparison of both structural features. Fig. 2c and d present the crystal structures of PTTO and the pyrochlore $Cd_2Nb_2O_7$, respectively.[40] Notably, PTTO and $Cd_2Nb_2O_7$ exhibit similar fundamental structural configurations. Moreover, the Ti/Te atoms in PTTO are located at the octahedral sites, which are occupied by Nb atoms in $Cd_2Nb_2O_7$. However, the coordination environments of the Pb atoms in PTTO and the Cd atoms in $Cd_2Nb_2O_7$ are noticeably different. The Pb atoms tend to exist in a highly distorted form of $[PbO_7]$ polyhedra. In contrast, the Cd atoms in $Cd_2Nb_2O_7$ are bonded to eight oxygen atoms, forming rigid $[CdO_8]$ polyhedra (Fig. 2e and f). This disparity between both the polyhedra leads to a change in the spatial symmetry of their structures, that $Cd_2Nb_2O_7$ crystallizes in the CS space group $Fd\bar{3}m$ and transforms into NCS space group $F\bar{4}3m$ in PTTO. Moreover, the calculated oxidation valence states of Pb, Ti/Te in PTTO were determined using BVS approach, yielding average values of +2.08 and +4.44, respectively. Also, XPS measurements are employed to precisely analyze the chemical states of the elements, as illustrated in Fig. 3a. Notably, the characteristic peaks at 586.3 and 576 eV were observed in PTTO, corresponding to the Te^{6+} cations (Fig. 3b). Moreover, the peaks detected at 142.8 and 137.9 eV were attributed to the Pb^{2+} cations (Fig. 3c), while those at 463.4 and 457.8 eV correspond to the Ti^{4+} cations (Fig. 3d).[41–43] The obtained valence states of the elements were found to be in good agreement with the structural data of PTTO.

Besides, the composition and distribution of the Pb, Ti, Te and O elements in PTTO were further ascertained according to EDS analyses. As depicted in Fig. S2,† the atomic molar ratio of Pb, Ti, Te and O was determined to be around 4.2: 2.8: 1: 12.9, respectively, closely consistent with the PTTO's structure analysis. The distribution mapping of these elements indicates a homogeneous distribution, further confirming the rationality of the crystal structure of PTTO.

Optical properties

The UV-vis-NIR diffuse reflectance spectra of PTTO polycrystals are shown in Fig. 4a, in which its UV absorption cutoff edge is observed at around 403 nm. According to the Kubelka–Munk formula, the band gap value of PTTO was determined to be 2.49 eV (inset of Fig. 4a). To obtain the IR absorption edge, the IR spectrum was recorded ranging from 400 to 4000 cm^{-1}. It is obvious from Fig. 4b that there are no significant absorption peaks within the broad range of 4000 to 730 cm^{-1}. Considering the multi-phonon absorption theory, it can be inferred that the infrared transmittance cutoff of PTTO is at 7.6 μm. Remarkably, the transmittance performance of this compound exceeds that of most commercially available oxide NLO crystals (<5 μm). Moreover, for a more rational evaluation of the IR transmittance performance of PTTO, we conducted a comparative analysis with tellurite compounds Li_2ZrTeO_6 and Li_2TiTeO_6, which have wide IR absorption edges exceeding 6.72 μm. As can be seen in Fig. 4b, the obvious IR absorption peaks in Li_2ZrTeO_6 and Li_2TiTeO_6 were observed at 718 and 760 cm^{-1}, respectively, notably higher than that of PTTO (650 cm^{-1}). Accordingly, this attribute highlights the potential of PTTO as an NLO crystal especially in the wide mid-IR wavelength region. Besides, a thorough examination of PTTO's IR spectrum absorption peaks reveals that the peaks observed at 652, 616 and 448 cm^{-1} correspond to the symmetric stretching and anti–stretching vibrations of the Te–O bond, while those near 500 cm^{-1} originate from the vibration mode of the Ti–O bond. These results align with earlier studies reported on

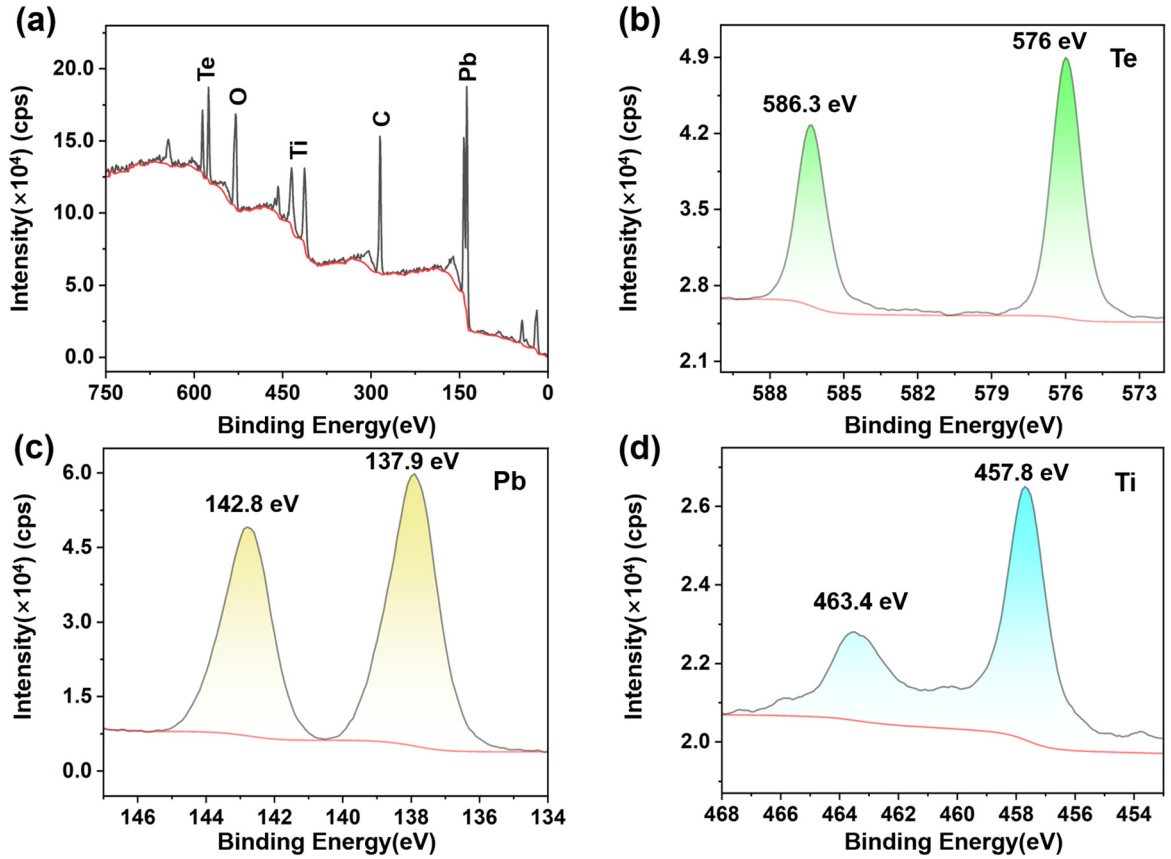

Fig. 3 (a) The survey XPS spectrum of the PTTO sample. (b–d) The element XPS spectra of Te, Pb and Ti, respectively.

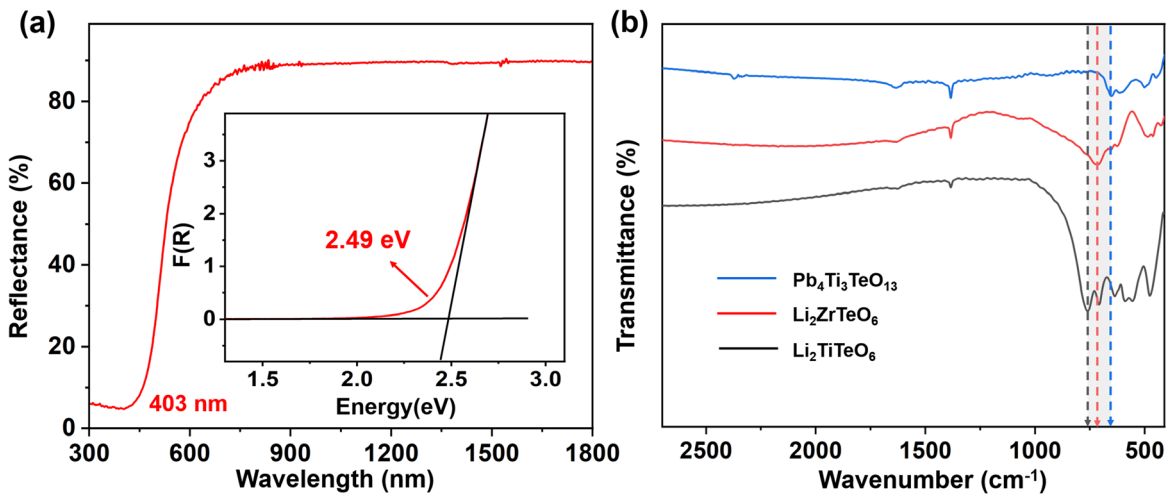

Fig. 4 (a) UV-vis-NIR diffuse reflectance spectrum and the corresponding band gap for PTTO. (b) A comparison of the IR spectra of PTTO, Li_2ZrTeO_6 and Li_2TiTeO_6.

these compounds, reinforcing the credibility of the experimental results.[44–46]

SHG measurement

To experimentally characterize the SHG behavior of PTTO, polycrystalline samples were subjected to illumination using a laser operating at a wavelength of 2 μm radiation. As a consequence of its crystallization in the cubic crystal system, PTTO was anticipated to demonstrate non-phase-matching behavior under the conditions of this experiment. Furthermore, Fig. S3† illustrates a comparison of the SHG intensity of PTTO and $AgGaS_2$ within the same particle size range of 100–150 μm.

Notably, the results revealed that PTTO exhibits a strong SHG intensity of 0.4 × $AgGaS_2$ under 2 μm laser radiation. Likewise, the cubic $CsCaBO_3$ and $K_6Cd_3(C_3N_3O_3)_4$ compounds demonstrate intense SHG effects of approximately 1 × and 3 × KDP, respectively.[47,48] These observations suggest that PTTO displays enhanced NLO properties despite its high level of symmetry.

Structure–property relationship

To elucidate the underlying origin of the substantial SHG activity exhibited by PTTO, a comprehensive analysis of the structure–property relationship was implemented utilizing first-principles calculations. As shown in Fig. 5, PTTO can be identified as an indirect bandgap semiconductor compound, as evidenced by the obvious disparity in the positions of the conduction band minimum and the valence band maximum within the Brillouin zone. The theoretically determined bandgap of PTTO (1.52 eV) is expected to be smaller than the corresponding experimental value (2.49 eV), primarily attributable to the inherent tendency of the GGA algorithm to underestimate bandgaps. Moreover, the analysis of density of states (DOS) and partial density of states (PDOS) results reveals that the top of the valence band is primarily occupied by Ti 3d and Pb 6p orbitals, while the electronic states at the bottom of the conduction band are predominantly contributed by O 2p, Ti 3d and Pb 6p orbitals (Fig. 5). As the optical characteristics of a material largely originate from electronic transitions in close proximity to the Fermi energy, it can be inferred that the observed NLO properties in PTTO mainly stem from the distorted $[TiO_6]$ octahedra and $[PbO_7]$ polyhedra. To further shed light on the role of the $[TiO_6]$ octahedra in the enhanced SHG effect in PTTO, an investigation utilizing the flexible dipole model was conducted as the positive correlation between the flexibility index and the strength of the SHG effect.[49] As respected, the analysis revealed a notable flexibility index of 0.132 for the $[TiO_6]$ octahedra in PTTO, which is close to that of $[ZrO_6]$ (0.146) octahedra in the NLO crystal Li_2ZrTeO_6 (Table S5†). This finding further highlights the influential role of the $[TiO_6]$ octahedra in enhancing the NLO activity in PTTO.

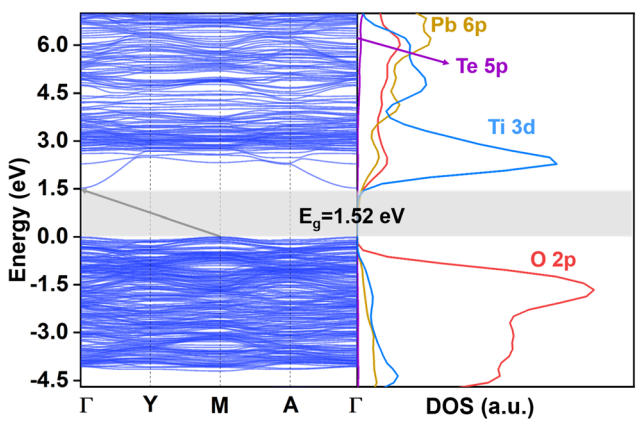

Fig. 5 Band structure and DOS analysis for the PTTO crystal.

Conclusions

In summary, we have successfully synthesized an acentric cubic lead titanium-tellurate crystal, PTTO, using flux methods. This compound features a distinctive pyrochlore-like 3D framework composed of the distorted $[Ti/TeO_6]$ octahedra and the $[PbO_7]$ polyhedra. Notably, powder SHG measurements revealed that PTTO displays a strong SHG intensity of 0.4 × $AgGaS_2$ under 2 μm laser radiation. Moreover, PTTO demonstrates a wide transparent window, with a UV absorption cutoff at 403 nm and an IR transparency cutoff at around 7.6 μm. Besides, first principles calculations and flexible dipole model analysis of SHG-active units provided an elucidation of the NLO activity exhibited by PTTO. These attributes highlight the potential of PTTO as a promising candidate for NLO applications with a wide transparency range.

Data availability

The data supporting this article have been included as part of the ESI.† Crystallographic data for 2374242† have been deposited at the CCDC.

Conflicts of interest

There are no conflicts to declare.

Acknowledgements

This work was financially supported by the National Natural Science Foundation of China (Grant No. 62475191, 22209201, and 52002273), the National Key R&D Program of China (2021YFA0717800), and the State Key Laboratory of Crystal Materials, Shandong University (No. KF2303).

References

1 P. S. Halasyamani and K. R. Poeppelmeier, Noncentro symmetric Oxides, *Chem. Mater.*, 1998, **10**, 2753–2769.
2 M. Mutailipu, K. R. Poeppelmeier and S. L. Pan, Borates: a rich source for optical materials, *Chem. Rev.*, 2021, **121**, 1130–1202.
3 X. Meng, K. Kang, F. Liang, J. Tang, W. Yin, Z. Lin and M. Xia, Optimal arrangement of π–conjugated anionic groups in hydro–isocyanurates leads to large optical anisotropy and second–harmonic generation effect, *Inorg. Chem. Front.*, 2020, **7**, 3674–3686.
4 X. Jiang, S. Deng, M. H. Whangbo and G. Guo, Material research from the viewpoint of functional motifs, *Natl. Sci. Rev.*, 2022, **9**, nwac017.
5 C. Wu, X. Jiang, L. Lin, Y. Hu, T. Wu, Z. Lin, Z. Huang, M. G. Humphrey and C. Zhang, A congruent–melting mid–infrared nonlinear optical vanadate exhibiting strong

Second–Harmonic Generation, *Angew. Chem., Int. Ed.*, 2021, **60**, 22447–22453.

6 C. Li, Z. Gao, P. Zhao, X. Tian, H. Wang, Q. Wu, W. Lu, Y. Sun, D. Cui and X. Tao, Crystallographic Investigations into the Polar Polymorphism of $BaTeW_2O_9$: Phase Transformation, Controlled Crystallization, and Linear and Nonlinear Optical Properties, *Cryst. Growth Des.*, 2019, **19**, 1767–1777.

7 T. Sasaki and A. Yokotani, Growth of large KDP crystals for laser fusion experiments, *J. Cryst. Growth*, 1990, **99**, 820–826.

8 X. Dong, L. Huang, C. Hu, H. Zeng, Z. Lin, X. Wang, K. M. Ok and G. Zou, $CsSbF_2SO_4$: An Excellent Ultraviolet Nonlinear Optical Sulfate with a $KTiOPO_4$ (KTP)–type Structure, *Angew. Chem., Int. Ed.*, 2019, **58**, 6528–6534.

9 C. Chen, B. Wu, A. Jiang and G. You, A new–type ultraviolet SHG crystal β–BaB_2O_4, *Sci. Sin., Ser. B*, 1985, **28**, 235–243.

10 C. Chen, Y. Wu, A. Jiang, B. Wu, G. You, R. Li and S. Lin, New nonlinear–optical crystal: LiB_3O_5, *J. Opt. Soc. Am. B*, 1989, **6**, 616–621.

11 C. Chen, G. Wang, X. Wang and Z. Xu, Deep–UV nonlinear optical crystal $KBe_2BO_3F_2$–discovery, growth, optical properties and applications, *Appl. Phys. B: Lasers Opt.*, 2009, **97**, 9–25.

12 V. Petrov, F. Rotermund, F. Noack and P. Schunemann, Femtosecond parametric generation in $ZnGeP_2$, *Opt. Lett.*, 1999, **24**, 414–416.

13 A. O. Okorogu, S. B. Mirov, W. Lee, D. I. Crouthamel, N. Jenkins, A. Y. Dergachev, K. L. Vodopyanov and V. V. Badikov, Tunable middle infrared downconversion in GaSe and $AgGaS_2$, *Opt. Commun.*, 1998, **155**, 307–312.

14 (*a*) X. Chen, H. Jo and K. M. Ok, Lead mixed oxyhalides satisfying all fundamental requirements for high–performance mid–infrared nonlinear optical materials, *Angew. Chem., Int. Ed.*, 2020, **59**, 7514–7520; (*b*) H. Yang, S. Zhou, M. Ran, X. Wu, H. Lin and Q. Zhu, Melilite oxychalcogenide $Sr_2FeGe_2OS_6$: a phase–matching IR nonlinear optical material realized by isomorphous substitution, *Inorg. Chem. Front.*, 2023, **10**, 2030–2038.

15 H. Lan, F. Liang, X. Jiang, C. Zhang, H. Yu, Z. Lin, H. Zhang, J. Wang and Y. Wu, Pushing nonlinear optical oxides into the mid–infrared spectral region beyond 10 μm: Design, synthesis, and characterization of $La_3SnGa_5O_{14}$, *J. Am. Chem. Soc.*, 2018, **140**, 4684–4690.

16 D. Lu, T. Xu, H. Yu, Q. Fu, H. Zhang, P. Segonds, B. Boulanger, X. Zhang and J. Wang, Acentric langanite $La_3Ga_{5.5}Nb_{0.5}O_{14}$ crystal: a new nonlinear crystal for the generation of mid–infrared parametric light, *Opt. Express*, 2016, **24**, 17603–17615.

17 W. Lu, Z. Gao, X. Liu, X. Tian, Q. Wu, C. Li, Y. Sun, Y. Liu and X. Tao, Rational design of a $LiNbO_3$–like nonlinear optical crystal, Li_2ZrTeO_6, with high laser–damage threshold and wide mid–IR transparency window, *J. Am. Chem. Soc.*, 2018, **140**, 13089–13096.

18 X. Du, X. Guo, Z. Gao, F. Liu, F. Guo, S. Wang, H. Wang, Y. Sun and X. Tao, Li_2MTeO_6 (M = Ti, Sn): Mid–infrared nonlinear optical crystal with strong second harmonic generation response and wide transparency range, *Angew. Chem., Int. Ed.*, 2021, **60**, 23320–23326.

19 K. Chen, C. Lin, G. Peng, Y. Chen, H. Huang, E. Chen, Y. Min, T. Yan, M. Luo and N. Ye, $LiNbTeO_5$: A high–performance multifunctional crystal material with a very large second harmonic generation response and piezoelectric coefficient, *Chem. Mater.*, 2022, **34**, 399–404.

20 Q. Wang, X. Dong, L. Huang, K. M. Ok, Z. Lin and G. Zou, $Cd_2Nb_2Te_4O_{15}$: A Novel Pseudo–Aurivillius–Type tellurite with unprecedented nonlinear optical properties and excellent stability, *Small*, 2023, **19**, 2302797.

21 F. Khachnaoui, N. B. Amor, M. Bejar, E. Dhahri and E. K. Hlil, Synthesis and magnetic properties of new pyrochlore $Fe_2Mn_2O_7$ compound, *J. Supercond. Novel Magn.*, 2018, **31**, 3803–3808.

22 J. A. Alonso and I. Rasines, On the influence of the non–bonded pair of Pb(II) in the novel ordered perovskite Pb $[Sc_{0.50}(Ti_{0.25}Te_{0.25})]O_3$, *J. Phys. Chem. Solids*, 1988, **49**, 385–389.

23 J. Xu, R. Xi, X. Xu, Y. Zhang, X. Feng, X. Fang and X. Wang, $A_2B_2O_7$ pyrochlore compounds: A category of potential materials for clean energy and environment protection catalysis, *J. Rare Earths*, 2020, **38**, 840–849.

24 Y. She, F. Liang, J. Jiao, W. Zhao, N. Ye, Z. Hu, Y. Wu and C. Li, A new stable polymorph of $Li_2TeMo_3O_{12}$ with wide midinfrared transparency and a large Raman response, *Inorg. Chem. Front.*, 2023, **10**, 3595–3604.

25 (*a*) J. Jiao, C. Li, Y. She, N. Ye, Z. Hu and Y. Wu, Achieving broadband ultraviolet to mid–infrared transparency in germanate–based nonlinear optical crystals $Cs_3REGe_3O_9$ (RE = Y, Gd), *Inorg. Chem. Front.*, 2023, **10**, 6869–6878; (*b*) Q. Wu, J. Zhou, X. Liu, X. Jiang, Q. Zhang, Z. Lin and M. Xia, $Ca_3(TeO_3)_2(MO_4)$ (M = Mo, W): Mid–Infrared Nonlinear Optical Tellurates with Ultrawide Transparency Ranges and Superhigh Laser–Induced Damage Thresholds, *Inorg. Chem.*, 2021, **60**, 18512–18520.

26 (*a*) W. Zhao, C. Li, T. Han, J. Jiao, Y. She, D. Ju, F. Liang, N. Ye, Z. Hu and Y. Wu, $Cs_2Bi_2OSi_2O7$: A promising bismuth silicate nonlinear optical crystal with face–sharing BiO_5 polyhedra exhibiting strengthened Second Harmonic Generation response and birefringence, *Chem. Mater.*, 2022, **34**, 3365–3372; (*b*) M. Xia, C. Tang and R. Li, $Rb_4Li_2TiOGe_4O_{12}$: A Titanyl Nonlinear Optical Material With The Widest Transparency Range, *Angew. Chem.*, 2019, **131**, 18425–18428.

27 M. Xia, X. Jiang, Z. Lin and R. Li, "All–Three–in–One": A new bismuth–tellurium–borate Bi_3TeBO_9 exhibiting strong Second Harmonic Generation response, *J. Am. Chem. Soc.*, 2016, **138**, 14190–14193.

28 M. Yan, H. Xue and S. Guo, Recent achievements in lone–pair cation–based infrared second–order nonlinear optical materials, *Cryst. Growth Des.*, 2021, **21**, 698–720.

29 J. Chen, C. Hu, F. Kong and J. Mao, High–performance Second–Harmonic–Generation (SHG) materials: new developments and new strategies, *Acc. Chem. Res.*, 2021, **54**, 2775–2783.

30 C. Li, Z. Gao, X. Tian, Q. Wu, F. Liu, X. Du, D. Huang, Y. Sun, D. Cui and X. Tao, Investigations into anisotropic properties of the nonlinear optical material $CdTeMoO_6$ with quasi–two–dimensional structure, *J. Alloys Compd.*, 2019, **777**, 59–66.

31 C. Cascales and I. Rasines, New pyrochlore $Pb_2^{II}[In_{0.5}Sb_{1.5}]O_{6.5}$, *Z. Anorg. Allg. Chem.*, 1985, **529**, 229–234.

32 W. Zhang, J. Sun, X. Wang, G. Shen and D. Shen, Crystal growth and optical properties of a noncentrosymmetric molybdenum tellurite, $Na_2Te_3Mo_3O_{16}$, *CrystEngComm*, 2012, **14**, 3490–3494.

33 G. M. Sheldrick, A short history of SHELX, *Acta Crystallogr., Sect. A: Found. Crystallogr.*, 2008, **64**, 112–122.

34 P. Kubelka and F. Z. Munk, Ein Beitrag zur Optik der Farbanstriche (Contribution to the optic of paint), *Z. Tech. Phys.*, 1931, **12**, 593.

35 S. K. Kurtz and T. T. Perry, A powder technique for the evaluation of nonlinear optical materials, *J. Appl. Phys.*, 1968, **39**, 3798–3813.

36 S. J. Clark, M. D. Segall, C. J. Pickard, P. J. Hasnip, M. J. Probert, K. Refson and M. C. Payne, First principles methods using CASTEP, *Z. Kristallogr.*, 2005, **220**, 567–570.

37 V. Milman, K. Refson, S. J. Clark, C. J. Pickard, J. R. Yates, S. P. Gao, P. J. Hasnip, M. I. J. Probert, A. Perlov and M. D. Segall, Electron and vibrational spectroscopies using DFT, plane waves and pseudopotentials: CASTEP implementation, *J. Mol. Struct.: THEOCHEM*, 2010, **954**, 22–35.

38 A. M. Rappe, K. M. Rabe, E. Kaxiras and J. D. Joannopoulos, Optimized pseudopotentials, *Phys. Rev. B: Condens. Matter Mater. Phys.*, 1990, **41**, 1227–1230.

39 J. A. Alonso, C. Cascales and I. Rasines, Preparation and crystal data of the New Pyrochlores $Pb_2[M_{1.5}Te_{0.5}]O_{6.5}$ (M = Ti, Zr, Sn, Hf), *Z. Anorg. Allg. Chem.*, 1986, **537**, 213–218.

40 T. Malcherek, U. Bismayer and C. Paulmann, The Crystal Structure of $Cd_2Nb_2O_7$: Symmetry Mode Analysis of the Ferroelectric Phase, *J. Phys.: Condens. Matter*, 2010, **22**, 205401.

41 C. K. Kang, S. U. Yuldashev, J. H. Leem, Y. S. Ryu, J. K. Hyun, H. S. Jung, H. J. Kim, T. W. Kang, H. I. Lee, Y. D. Woo and T. W. Kim, Surface Passivation by Sulfur Treatment of Undoped *p*–CdTe (100), *J. Appl. Phys.*, 2000, **88**, 2013–2015.

42 Q. Zhang, H. Zhu, B. Yang, F. Jia, H. Yan, M. Zeng and H. Qu, EFFECT of Pb^{2+} on the flotation of molybdenite in the presence of sulfide ion, *Results Phys.*, 2019, **14**, 102361.

43 M. Qiao, J. Wang, D. Wei, J. Li, X. Lei, W. Lei, J. Wei and Q. Zhang, Influence of crystalline phase evolution of shells on microwave absorption performance of core–shell Fe_3O_4@TiO_2 nanochains, *Mater. Today Nano.*, 2022, **18**, 100203.

44 J. Wang, H. Wu, H. Yu, Z. Hu, J. Wang and Y. Wu, $LaTeBO_5$: a new borotellurite with a large birefringence activated by the highly distorted $[Te^{(iv)}O_4]$ group, *Dalton Trans.*, 2021, **50**, 12404–12407.

45 Z. Li, S. Zhang, W. Yin, Z. Lin, J. Yao and Y. Wu, $Na_3Ca_4(TeO_3)(PO_4)_3$: A New Noncentrosymmetric Tellurite Phosphate with Fascinating Multimember–Ring Architectures and Intriguing Nonlinear Optical Performance, *Dalton Trans.*, 2018, **47**, 17198–17201.

46 F. Bonhomme, J. P. Larentzos, T. M. Alam, E. J. Maginn and M. Nyman, Synthesis, structural characterization, and molecular modeling of dodecaniobate Keggin chain materials, *Inorg. Chem.*, 2005, **44**, 1774–1785.

47 M. Wen, H. Wu, X. Su, J. Lu, Z. Yang, X. Wu and S. Pan, $ACaBO_3$ (A = Cs, Rb): two new cubic borates with isolated BO_3 groups, *Dalton Trans.*, 2017, **46**, 4968–4974.

48 M. Xia, M. Zhou, F. Liang, X. Meng, J. Yao, Z. Lin and R. Li, Noncentrosymmetric Cubic Cyanurate $K_6Cd_3(C_3N_3O_3)_4$ Containing Isolated Planar π–Conjugated $(C_3N_3O_3)^{3-}$ Groups, *Inorg. Chem.*, 2018, **57**, 32–36.

49 X. Jiang, S. Zhao, Z. Lin, J. Luo, P. D. Bristowe, X. Guan and C. Chen, The role of dipole moment in determining the nonlinear optical behavior of materials: *ab initio* studies on quaternary molybdenum tellurite crystals, *J. Mater. Chem. C*, 2014, **2**, 530–537.